JACS
JOURNAL OF THE AMERICAN CHEMICAL SOCIETY
Article
Cite This: J. Am. Chem. Soc. 2017, 139, 15337-15346
pubs.acs.org/JACS

Bioengineering a Single-Protein Junction

Marta P. Ruiz,[†,‡,§] Albert C. Aragonès,[†,‡,§] Nuria Camarero,[‡,§] J. G. Vilhena,[#,○] Maria Ortega,[#] Linda A. Zotti,[#] Rubén Pérez,[*,#,Δ] Juan Carlos Cuevas,[#,Δ] Pau Gorostiza,[*,‡,§,∥] and Ismael Díez-Pérez[*,†,‡,§]

[†]Departament of Materials Science and Physical Chemistry & Institute of Theoretical and Computational Chemistry (IQTCUB), University of Barcelona, Martí i Franquès, 1, Barcelona 08028, Spain

[‡]Institute for Bioengineering of Catalonia (IBEC), The Barcelona Institute of Science and Technology (BIST), Baldiri Reixac 15-21, Barcelona 08028, Spain

[§]Centro Investigación Biomédica en Red (CIBER-BBN), Campus Río Ebro-Edificio I+D, Poeta Mariano Esquillor s/n, 50018 Zaragoza, Spain

[∥]Catalan Institution for Research and Advanced Studies (ICREA)

[#]Departamento de Física Teórica de la Materia Condensada, Universidad Autónoma de Madrid, E-28049 Madrid, Spain

[○]Department of Macromolecular Structures, Centro Nacional de Biotecnología, Consejo Superior de Investigaciones Científicas, 28049 Cantoblanco, Madrid, Spain

[Δ]Condensed Matter Physics Center (IFIMAC), Universidad Autónoma de Madrid, E-28049 Madrid, Spain

Supporting Information

ABSTRACT: Bioelectronics moves toward designing nanoscale electronic platforms that allow *in vivo* determinations. Such devices require interfacing complex biomolecular moieties as the sensing units to an electronic platform for signal transduction. Inevitably, a systematic design goes through a bottom-up understanding of the structurally related electrical signatures of the biomolecular circuit, which will ultimately lead us to tailor its electrical properties. Toward this aim, we show here the first example of bioengineered charge transport in a single-protein electrical contact. The results reveal that a single point-site mutation at the docking hydrophobic patch of a Cu-azurin causes minor structural distortion of the protein blue Cu site and a dramatic change in the charge transport regime of the single-protein contact, which goes from the classical Cu-mediated two-step transport in this system to a direct coherent tunneling. Our extensive spectroscopic studies and molecular-dynamics simulations show that the proteins' folding structures are preserved in the single-protein junction. The DFT-computed frontier orbital of the relevant protein segments suggests that the Cu center participation in each protein variant accounts for the different observed charge transport behavior. This work is a direct evidence of charge transport control in a protein backbone through external mutagenesis and a unique nanoscale platform to study structurally related biological electron transfer.

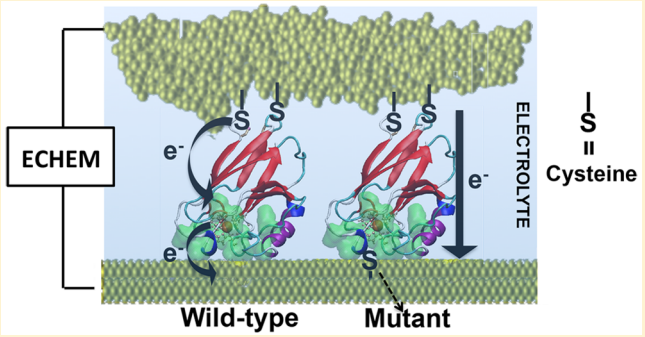

INTRODUCTION

Biological electron transfer (ET) is the key step in many basic cellular processes such as respiration and photosynthesis.[1] Nature has developed highly specialized molecular building blocks capable of transporting charge with unprecedented efficiency, i.e., fast and at long distances.[2,3] Understanding the mechanisms behind biological ET is key to elucidate the changes in the charge transport regime caused by specific structural variations of the associated molecular machinery, which ultimately lead to, for instance, malfunctioning of the mitochondria. Such subtle ET changes are typically caused by specific mutations of one or more residues in the involved ET proteins, and they have been directly linked to well-described severe pathologies related to the overproduction of reactive oxygen species.[4−6]

Fundamental knowledge is not the only gain from studying biological ET. Such knowledge can also be exploited to design bioelectronic devices. Such studies would ultimately unveil what are the key parameters to be controlled in the transduction of electrical signals from active biomolecules, and direct us, for instance, to the design of the next generation of highly specific optoelectronic sensors.[7,8] In order to comply with the increasingly demanding downsizing of the microelectronics industry, the latest bioelectronic advances focus

Received: June 13, 2017
Published: October 5, 2017

DOI: 10.1021/jacs.7b06130
J. Am. Chem. Soc. 2017, 139, 15337−15346

mainly on bottom-up perspectives,[8] aiming for maximum sensitivities, high signal-to-noise ratios, and enhanced efficiency in order to reduce energy consumption.

Several ubiquitous redox proteins in biological ET have become model biomolecular systems to study, owing to their structural robustness against mutagenesis.[9] These systems have also been suggested as versatile building blocks in molecular electronic devices such as logic gates and multistate memory devices.[10−12] The structural similarity between the two redox states of the metal center in most model redox proteins provides a functional advantage, as the characteristic reorganization free energy (λ) for the redox ET is kept within low values, 0.6−0.8 eV,[13,14] allowing high ET rates.[9] The exact atomistic origin of such structural invariability that leads to low λ values has been a longstanding debate.[15,16] Redox proteins also present a large tunability of their redox potentials at minor structural costs. Many studies have dug into the redox potential control of metalloproteins by means of point-site mutations in order to correlate it with the molecular structure.[17,18] The redox midpoint potential exhibited by the band c-type cytochromes varies between −400 and 400 mV vs a normal hydrogen electrode (NHE) upon specific chemical modification of the Fe-heme surrounding.[19] The reactivity and associated function of ET proteins depend critically on its redox potential, whose value is greatly affected by differences in the first coordination sphere of the metal center.[20,21] For example, it has been shown in blue-copper proteins that a shorter (stronger) axial Cu(II)−S(thioether) bond (as opposed to a longer (weaker) Cu(II)−S(thiolate) bond) results in a green site (as opposed to the blue site). This difference results in a tetragonally distorted structure, thus substantially modifying the redox potential of the protein.[20,22] Not only mutations at the residues closer to the protein metal site are responsible for such redox tunability. It has been demonstrated that modifications of the secondary coordination sphere in Cu proteins can widely affect the protein redox potential through controlling the hydrophobicity and hydrogen-bonding interactions.[17,23] Such large potential tunability through point mutations of the outer protein sphere highlights the profound importance of the redox potential control of biological molecules in carrying out a wide variety of bioenergetic processes.[24]

Model redox proteins have been integrated in nano/microscale devices as the charge transport material. Cu-azurin conductance signatures have been recently observed in microscale solid-state devices,[25−27] which demonstrates their compatibility when hybridized to an electronic platform. Redox protein models such as Cu-azurin and cytochrome b_{562} have also been extensively analyzed at the single-protein level by several groups.[28−34] These pioneering studies established a metal-mediated electron transport through the metalloprotein, which has been usually pictured as to the electron jumping from one electrode terminal to the Cu(II) metal center and, sequentially, from the Cu(I) center to the second electrode.[28] The exact details of this mechanisms are, however, under debate.[34,35] With independence of the exact mechanistic details, these works demonstrated the feasibility of such hybrid biointerfaces to work as active components in nanoscale circuits. We have recently exploited these capabilities to build single-protein junctions displaying unique electrical signatures by profiting from their exceptional redox properties, namely, a low operational voltage field-effect transistor[36] and a redox conductance-switching device.[37]

Here we present an example of bioengineering charge transport in a single-protein junction. The copper-binding protein azurin from *Pseudomonas aeruginosa* has been exploited to compare charge transport of single-protein electrical contacts made of a wild-type (Wt) structure and a mutant (K41C), where, in the latter, the natural lysine (*Lys*) 41 residue has been replaced by a cysteine (*Cys*) (Figure 1a). This single point mutation has a twofold effect; first, the new solvent-exposed thiol (−SH) group will serve as a new chemical connection to one of the external electrode terminals, and second, the modification is in the secondary coordination sphere of the Cu

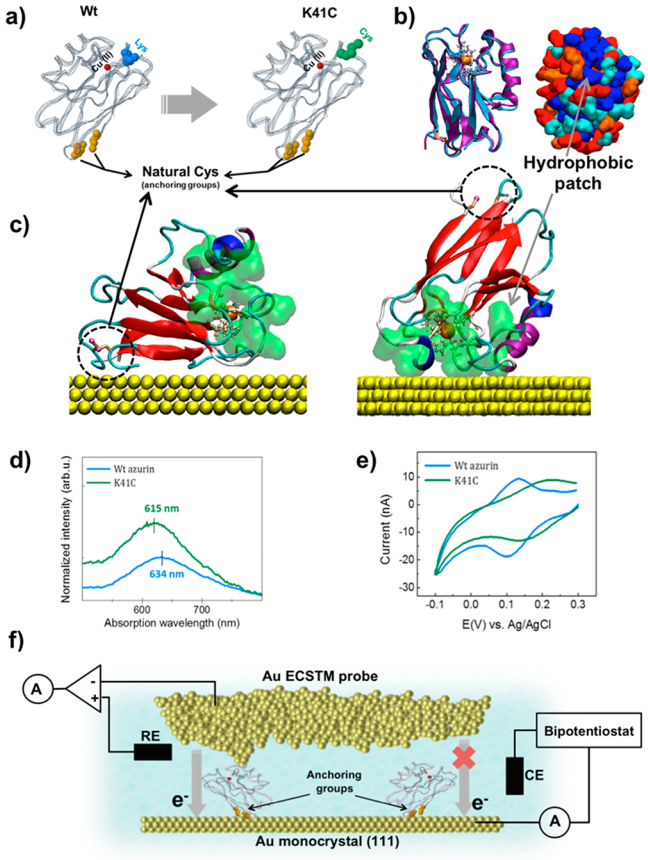

Figure 1. Structural assessment of the proteins and scheme of the single-protein junction setup. (a) Structural models of the studied wild-type azurin (left structure extracted from the Protein Data Bank (PDB)[40]) and its K41C variant (right structure). Natural cysteines (*Cys*3 and *Cys*26) are colored in orange. The wild-type amino acid *Lys*41 (blue) was substituted by a *Cys*41 (green) through a point-site mutation. (b) Superimposed structures of WT (cyan) and K41C (magenta) after a 500 ns molecular dynamics simulation (left panel). Representation of the same orientation of the surface hydrophobic/philic residues of the wild-type azurin (right panel, color legend: blue-cyan-orange-red ranges from very hydrophobic to very hydrophilic). (c) Stable adsorption configurations of the wild-type over a Au substrate after 150 ns molecular dynamics simulation. The hydrophobic pocket is represented with a transparent green Connolly surface. (d) Absorption spectra of the wild-type (blue trace) and the K41C (green trace) in ammonium acetate buffer (pH 4.55). (e) Electrochemical cyclic voltammetry response of the two protein variants adsorbed on a functionalized Au(111) substrate in 50 mM ammonium acetate buffer (pH 4.55). The electrochemical potential scan rate was set to 50 mV/s (see further details in the Supporting Information, section 4). (f) Schematic representation of the single-protein junction using an EC-STM setup.

DOI: 10.1021/jacs.7b06130
J. Am. Chem. Soc. 2017, 139, 15337−15346

center, which is expected to influence the metal redox behavior[17,23] and, hence, the transport regime through the protein matrix. Individual proteins of both variants were trapped between two metal electrodes in a physiological environment using an electrochemical scanning tunneling microscope (EC-STM) configuration, and the charge transport was characterized as a function of an applied electrochemical gate voltage and temperature. We have successfully implemented a static *blinking* modality in the past[38,39] that has been exploited here to preserve the folding structure of the protein during the single-molecule transport measurements. All-atom molecular-dynamics (MD) simulations suggest that the electrode−protein−electrode junction occurs via two well-localized sites on the protein, i.e., the hydrophobic patch and the natural *Cys* residues. Despite that comparable orientations of both Wt and K41C proteins bridges are expected, the results show acute differences in the charge transport mechanism of the single-protein junction between the Wt and the mutant variant, observing in the latter a complete shutdown of the two-step sequential tunneling character typically described in the Wt.[28] *Ab initio* calculations of the relevant ET pathway fragment including the modified residue 41 show the poor participation of the Cu center in the transport-relevant molecular frontier orbital of the K41C mutant. These results fully account for the observed conduction changes within the framework of the coherent tunneling mechanism for the single-protein junction of the bioengineered protein.

RESULTS AND DISCUSSION

Experimental Characterization and Molecular Dynamics Simulations for the Assessment of the Mutant's Structure and Activity. Details on the protein expression and purification including the Wt and the K41C mutant (Figure 1a) can be found in the Experimental and Computational Methods section and in the Supporting Information, section 2. The proteins' structures in Figure 1a have been both represented on the basis of the Wt crystalline structure. Despite the lack of crystalline structure of the K41C mutant, this section shows firm evidence of both the preservation of its folding structure and electrical activity. We have first run exceedingly long (500 ns) molecular dynamics (MD) simulations for the entire protein structure immersed in an aqueous medium and seen no major structural changes after introducing the mutation at the 41 position (see Figure 1b and the Supporting Information, section 7b), which assesses the robustness of the Cu-azurin structure against modifications of its outer sphere. This result is consistent with the findings obtained in other single point mutants of azurin for which the crystal structure exists.[17] On top of the MD results, Figure 1d shows the UV−visible absorption spectra for the Wt Cu-azurin and its K41C variant in the working ammonium acetate buffer, both displaying strong ligand-to-metal charge transfer (LMCT) absorption bands within the range of the typical Cu proteins blue site, 634 and 615 nm, respectively, for Wt and K41C. The exact position of these bands has been extensively used to extract details on the Cu ligand-field structure in blue Cu proteins upon specific mutations. The observed slight blue shift for the K41C suggests a small perturbation of the Cu binding site upon mutation,[17,21] which is ascribed to a decrease in the ligand-field energy as a result of the axial coordination weakening of the methionine (Met) 121 residue binding the Cu metal center.[20,22] This different "energetics" of the chemical surrounding for the Cu center has direct impact on the protein redox properties. A decrease in the ligand-field energy typically worsens the stability of the Cu(II) oxidation form because the −S coordination to the *Met* elongates, thus destabilizing the oxidized Cu form and raising the protein redox potential.[17,22,41] Figure 1e shows the cyclic voltammograms of both Wt and K41C variants of the Cu-azurin adsorbed on a Au(111) surface (see the Experimental and Computational Methods section and the Supporting Information, section 4, for more details). The electrode surface functionalization conducted to record the voltammogram of the proteins (see Figure S4a) assures the conformation of both proteins with the hydrophobic patch facing the Au electrode. In agreement with the spectroscopic signal, the measured mid-redox potential displays an anodic shift of ∼50 mV for the K41C mutant with respect to the Wt, which points to a destabilization of the Cu(II) oxidation state. Moreover, the larger cathodic (U_{red})-to-anodic (U_{ox}) peaks separation ($U_{ox}-U_{red}$ of 0.038 and 0.096 V for the Wt and K41C, respectively) evidences a reversibility loss in the K41C mutant versus the Wt,[42] owing to the stabilization of one of the Cu oxidation states and implying a markedly slower electron transfer rate in the electrochemical channel. Finally, the folding state of the K41C mutant structure has been tested out by measuring the extension of the fluorescence quenching of the inner tryptophan (*Trp*) 48 residue.[43] The fluorescence emission around 310 nm for the K41C variant evidences a correct folding of its structure (see details in the Supporting Information, section 3).

Electrochemical Gate-Dependent Single-Protein Transport. We have formed and electrically characterized single-protein junctions in a physiological environment (ammonium acetate buffer pH 4.5) for both target systems, i.e., the Wt and the K41C variant. To this aim, the target proteins are absorbed onto a clean Au(111) electrode surface and an electrochemical scanning tunneling microscope (EC-STM) break-junction approach is used to bridge individual proteins between both the Au(111) substrate and the Au STM tip electrodes under electrochemical control (Figure 1f). The 150 ns MD simulations under the same working conditions (see the Supporting Information, section 7b) show that Cu-azurin adsorption to gold occurs either through the naturally present *Cys* residues or through the hydrophobic patch (Figure 1c), which reinforces the pre-established idea that the contact between the tip-protein-surface occurs via these two sites,[36,44] i.e., STM tip-hydrophobic-patch/*Cys*-surface or *vice versa*. In addition, our simulations confirm that the process of adsorption occurs with a minor loss of the secondary structure of the protein (Supporting Information, section 7b), in agreement with the measured electrochemical activity for both systems (Figure 1e). Both simulations and experiments indicate that the protein attachment to a Au substrate is stable and allows imaging individual redox-active proteins on the electrode surface for long time periods of up to several hours (see the Supporting Information, section 5). A similar anchoring geometry will be expected for the K41C mutant given that this residue is located in the hydrophobic patch, one of the two preferential adsorption sites observed for the Wt. In order to validate this assumption, we have performed two additional MD simulations concerning the adsorption of the K41C and Apo-azurin over gold along the orientation O1. The results are presented in Figure S23 and show that, in the three cases (i.e., Wt-Holo, K41C, and Wt-Apo), the final adsorption configuration is very similar, thus strengthening our hypothesis that this point mutation will not produce significant modifications in

DOI: 10.1021/jacs.7b06130
J. Am. Chem. Soc. 2017, 139, 15337−15346

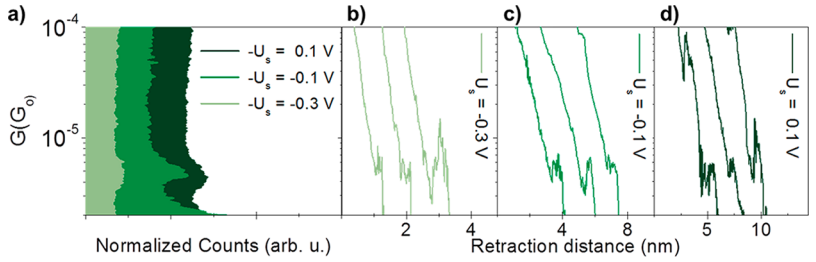

Figure 2. *Dynamic* single-protein transport of the K41C junction. (a) Conductance histograms at three extreme EC gate potentials ($-U_{Sample}$ in our EC-STM configuration) covering the redox potential window for the K41C protein. The histograms were built out of hundreds of retracting curves (conductance (G) vs retraction distance (nm)) from the break junction experiments displaying quantum conductance plateau features. (b–d) Three representative retracting curves containing plateau features at the three applied EC gate potentials (dark gray 0.1 V, black −0.1 V, light gray −0.3 V). An offset was applied in the *X*-axis in all plots for better visualization. A constant 300 mV voltage bias ($V_{bias} = U_{sample} - U_{tip}$, where U_{sample} and U_{tip} are the Au substrate and STM tip electrochemical potentials, respectively) was applied.

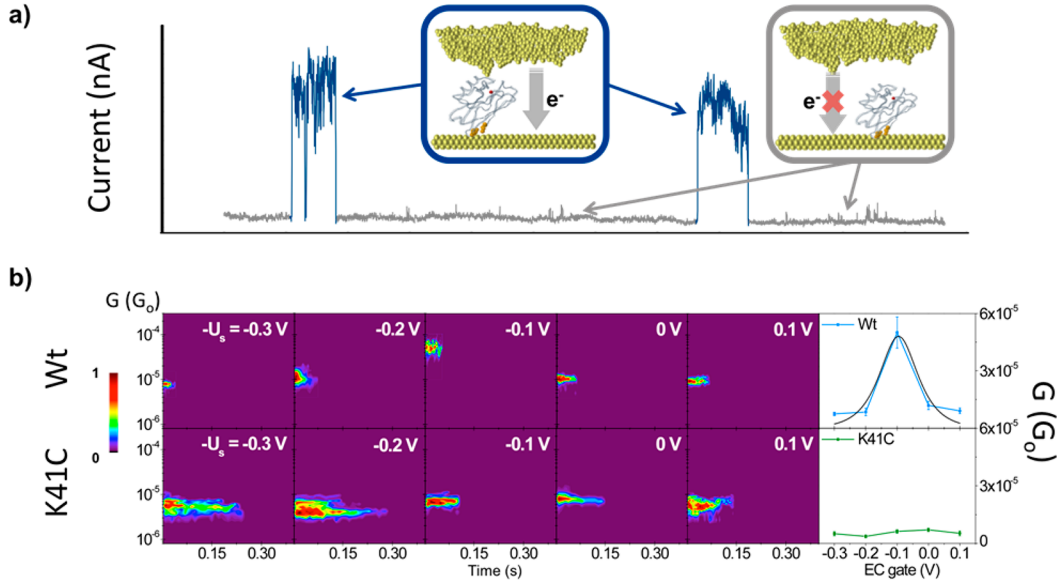

Figure 3. Gate-dependent single-protein transport. (a) Representative "*blinks*" (blue traces) identified in the transients of the current flowing between the two electrodes at a constant distance (2–3.5 nm) and V_{bias} (300 mV). Such *blinks* are observed when a protein spans the gap between the EC-STM tip and the Au substrate electrodes. When the protein disconnects from one of the electrodes, the current drops down to the initial set point level. $G = I_{step}/V_{bias}$ is used to obtain the conductance values. (b) Semilog 2D-blinking maps for both proteins (Wt top and K41C bottom) at different EC gate potentials. Several tens (up to a hundred) of individual blinking traces like that shown in part a are accumulated to build each 2D map without any selection. The counts have been normalized for each map versus the maximum value so that each 2D map has its maximum count set to 1. The far right graphs summarize the average single-protein conductance (G) vs the EC gate (V) for both studied proteins. The average conductance values were obtained from the Gaussian fits of the maxima in the vertical 1D histogram for each 2D map (see Figure S8 in the Supporting Information, section 5). The error bars in these plots are extracted from the full width at half-maximum (fwhm) of the Gaussian fits.

the final adsorption configuration and, therefore, it shall not alter the contact surface-protein-tip obtained for the Wt-Holo azurin.

The break-junction approach is operated in two different modalities, namely, dynamic *tapping* and static *blinking*. In the former, the STM tip is continuously approached and retracted to/from the Au electrode substrate where the target protein is anchored. When an individual protein binds the STM tip electrode and closes the gap, a single-protein junction is formed, displaying a typical quantum conductance plateau feature in the current versus distance retracting curve.[45] Hundreds of such retracting curves (Figure 2b–d) are then accumulated into a single conductance histogram for each particular applied electrochemical potential (Figure 2a). We have previously demonstrated the feasibility of this method to study the charge transport in a single-azurin (Wt) junction as a function of the applied electrochemical (EC gate) potential[36] (EC gate = $-U_{sample}$, where U_{sample} is the substrate electrochemical potential). Figure 2 shows the dynamic measurements of the single-protein transport conductance values of the K41C mutant as a function of the applied EC gate. In stark contrast with the Wt behavior, the single-protein junction of the K41C mutant shows no transistor behavior; i.e., the conductance is invariable versus the EC gate within the relevant redox potential window. The transport behavior in the Wt is characterized by a two-step sequential tunneling that results in a maximum in the conductance versus EC gate curve,[29,36] and suggests a direct tunneling transport in the K41C mutant.[25]

Single-biomolecular transport results by means of the dynamic STM break-junction approach has been previously shown in many instances.[32,36,46−49] However, the force exerted over the folding structure of the biomolecule in every pulling cycle (Figure 2b–d) might disrupt its structure and lead to a misinterpretation of the single-biomolecule transport data.

DOI: 10.1021/jacs.7b06130
J. Am. Chem. Soc. 2017, 139, 15337−15346

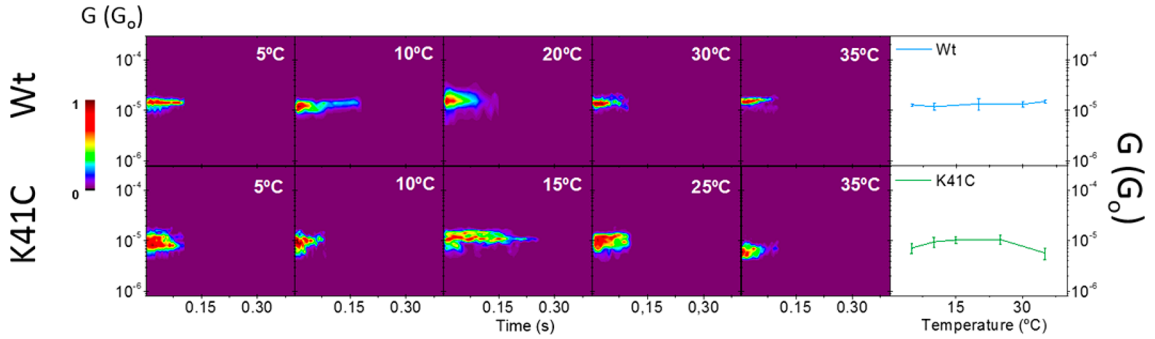

Figure 4. Temperature-dependent single-protein transport. Semilog 2D-blinking maps for both proteins (Wt top and K41C bottom) at different temperatures (from 5 to 35 °C), constant distance (2 to 3.5 nm) and V_{bias} (300 mV). The applied EC gate value was set to 0 and −100 mV for Wt and K41C mutant, respectively. The counts have been normalized for each map versus the maximum value, so each 2D map has its maximum count set to 1. The far right graph summarizes the single-protein conductance (G) vs temperature (°C) for both studied proteins. The average conductance values were obtained from the maxima Gaussian fits in the vertical 1D histogram for each 2D map (see Figure S9 in the Supporting Information, section 5). The error bars in these plots are extracted from the full fwhm of the Gaussian fits.

Here we rule out this uncertainty by using a static version of the EC-STM break-junction approach, namely, the *blinking* mode[39,50] (see more details in the Supporting Information, section 5). Briefly, the STM tip electrode is initially approached to the Au(111) substrate where the proteins have been preadsorbed to a distance of 1.5−2 nm, which is achieved by imposing a small (∼100 pA) tunneling current set point at an applied bias voltage difference between the two electrodes (bias voltage (V_{bias}) = U_{sample} − U_{tip}). Once the STM tip-to-substrate gap is mechanically stable, the current feedback loop is turned off and the tunneling current is monitored. Spontaneous trapping of proteins between both Au electrodes results in a telegraphic noise in the measured tunneling current flowing between the electrodes, which appears in the form of sudden "jumps" (*blinks*) (Figure 3a).[39,51] In order to corroborate that the observed *blinks* correspond to protein trapping events, larger electrode−electrode separations (up to 3.5 nm) were imposed by retracting the STM tip electrode further away from the surface. We observe that the large protein backbone (∼4 nm) is still capable of closing large electrode−electrode gap separations, resulting in a similar telegraphic signal (see the Supporting Information, section 5), yet at lower success rates. In support of this picture, we have run MD simulations of an STM tip approaching a Wt azurin stably absorbed on the Au(111) substrate (see the Supporting Information, section 7) and observed that the protein folding structure remains stable even after the STM tip establishes physical contact to it at distances close to 2.5 nm (see the Supporting Information movie and Supporting Information, section 7b).

Figure 3b panels show the accumulation of tens of such *blinking* traces into single 2D maps at different applied EC gate potentials for the Wt (top panel) and the K41C mutant (bottom panel). Such 2D *blinking* maps[39,52] are built by setting all *blinking* features from individual current transients (Figure 3a) to a common time origin and subtracted tunneling background, and represent solely the net conductance flowing through the protein junction. The horizontal fringe observed in the 2D blinking maps represents the conductance dispersion of the single-protein junction, whose average values are represented as a function of the applied EC gate in the far right graph of Figure 3b. Comparable conductance values are obtained from the static 2D maps (Figure 3b) and the dynamic break-junction histograms (Figure 2) for the K41C variant, 5 × $10^{-6}G_0$ and 3 × $10^{-6}G_0$ respectively (G_0 = 77.5 μS), being on average slightly larger in the former, which might evidence the detrimental effect of the protein "stretching" in the latter method. The single-protein conductance in Figure 3b for the K41C follows the same nondependent EC gate behavior observed in the dynamic break-junction experiments (Figure 2), with a slightly lower off-resonance current (at an EC gate voltage of −0.3 V) when compared to the single-Wt junction (Figure 3b, upper panel). As expected in the latter case, a maximum in the conductance versus the EC gate potential near the mid-redox value is observed for the Wt (Figure 3b, far right panel)[36] as opposed to the invariability for the single-K41C mutant junction conductance behavior within the same relevant redox potential range. These results suggest a sharp change in the transport behavior of the single-protein electrical contact, going from a classic sequential two-step tunneling for the Wt, observed in a number of other redox molecular junctions,[36,53,54] to a fully coherent tunneling for the K41C mutant. A numerical version of the two-step tunneling model is given in eq 1 and expresses the enhanced current (I_{enh} in nanoamps) flowing through the molecular junction[53]

$$I_{enh} = 1820V_{bias}[e^{((2898/\lambda T)(\lambda+\xi\eta+\gamma V_{bias})^2)} + e^{((2898/\lambda T)(\lambda+V_{bias}-\xi\eta-\gamma V_{bias})^2)}]^{-1} \quad (1)$$

where ξ and γ are model parameters ranging between 0 and 1 describing the fraction of the overpotential η in volts (η = U_{sample} − U_{redox}, where U_{redox} corresponds to the protein redox midpoint extracted from Figure 1e) and the V_{bias} (in volts) felt by the reactive redox center in the molecular junctions, respectively. T (in °C) is the temperature, and λ (in eV) is the reorganization energy (the energy difference between the oxidized and reduced states of the protein). All other physical constants have been numerically processed for simplicity taking reasonable assumptions of our experimental setup such as fully adiabatic limit (strong molecule/electrode coupling), fixed junction geometry for every measured *blink*, Au as electrode material, and aqueous solution as the environment. A fit of the Wt experimental results (blue trace in Figure 3b, far left graph) yields reasonable values for λ, ξ, and γ, 0.27 eV, 0.95, and 0.79, respectively,[28,36] evidencing low reorganization energies, large EC gating efficiencies, and a slight asymmetric V_{bias} distribution due to the usually asymmetric location of the Cu center in the molecular junction. It is important to note that the two-step sequential tunneling model fits the current versus the EC gate

DOI: 10.1021/jacs.7b06130
J. Am. Chem. Soc. 2017, 139, 15337−15346

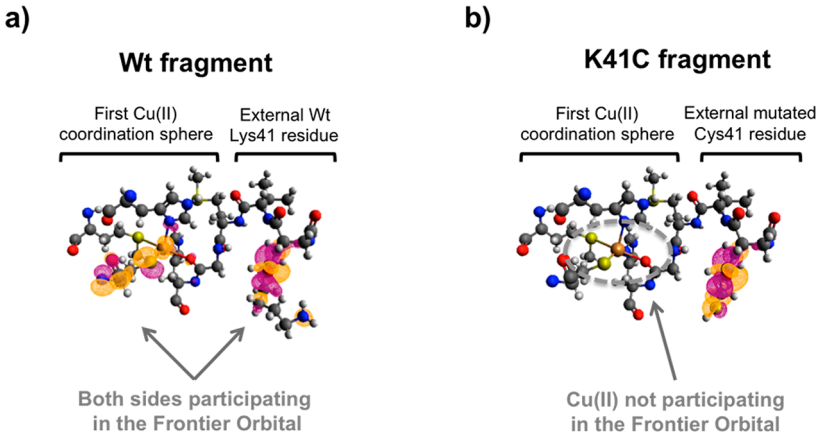

Figure 5. Electronic structure calculations. Isosurface plots (isovalue = 0.02) of the lowest unoccupied frontier molecular orbital (LUMO) involved in the electron transport of (a) Wt and (b) K41C fragments. Calculations were done at the CAM-B3LYP/6311G+(d) level of DFT.

voltage behavior, but it is not used to evaluate the absolute values of the current flowing through the single-protein junction. Accurate calculated values of the current flowing through the protein junction would require the introduction of coupling terms to both junction electrodes, which are difficult to model given the lack of information on the protein/electrode contact geometry.

Another relevant piece of information that can be extracted from the 2D blinking map is related to the characterization of the single-protein junction lifetime (*X*-axis in Figure 3b). In general, larger lifetime values for the K41C mutant are observed (see full lifetime statistics in the Supporting Information, section 5), which points toward a more stable protein/STM tip thiol bond thanks to the newly introduced *Cys*41 residue. The slight lifetime differences among the applied EC gate voltages might be due to different electrostatic stabilization of the thiol bond at the Au/protein interface and need to be further studied. In support of the general single-protein junction stabilization for the K41C, we have functionalized Au nanoparticles (NPs) with both Wt and K41C variants and detected a significantly larger percentage of multimeric Au NP structures in the latter (see the Supporting Information, section 6), evidencing the enhanced K41C bridging capability. Such a configuration leads to a similar metal/protein/metal orientation in the K41C junction as compared to the Wt protein (see the Supporting Information, section 7).

Temperature-Dependent Single-Protein Transport. In order to search for possible sources of fully incoherent transport in any of the studied single-protein junctions (i.e., hopping transport regime[55,56]), we have conducted single-protein transport measurements as a function of temperature. Figure 4 shows the temperature-dependent single-protein conductance results for both proteins at EC gate potentials of 0 and −100 mV for the Wt and the K41C mutant, respectively, near their respective redox midpoint potentials. The temperature range covers the room temperature conditions and approaches physiologically relevant values (∼37 °C).[57] The maximum temperature values were kept below 40 °C to prevent any denaturalization of the protein structures (84.4 °C for the Wt[58] and >70 °C for the K41C (see the Supporting Information, section 3b). Temperature-dependent single-protein conductance experiments are subjected to severe mechanical instabilities originated by thermal drift, which prevents reliable evaluation of the single-protein junction lifetime, usually resulting in similar values for both protein variants. The invariance of the single-protein junction conductance versus temperature in both proteins rules out any fully incoherence source of transport within the relevant temperature range and underscores the important fact that the protein is able to maintain a high level of coherence even for very different transport regimes, namely, two-step sequential and direct tunneling. Similar behavior has also been observed in microscale solid-state devices sandwiching a Wt azurin protein.[25] The temperature-dependent conductance within the two-step sequential scenario (see eq 1) shows a very shallow trend as we approach the $\eta = 0$ point ($U_{sample}=U_{redox}$), at which the measurements were performed (see the Supporting Information, section 7c, where the temperature dependence of eq 1 is represented at different η values). Building upon this mechanistic analysis, the conductance invariance of the K41C single-protein junction against both EC gate potential and temperature suggests a complete loss of the Wt sequential tunneling character, turning into a fully coherent tunneling regime.[59]

Computational Studies of the Electronic Properties. To understand the observed transition in the charge transport regimes between the two studied single-protein junctions, we have performed *ab initio* computational calculations in the structurally relevant proteins segment for charge transport. We have used DFT computational methods (see the Supporting Information, section 7, and the Experimental and Computational Methods section for more details) using the long-range corrected B3LYP functional (CAM-B3LYP) to visualize the distribution of the frontier orbitals nearby the redox active Cu(II) metal center for the Wt azurin and the K41C variants. Due to the intrinsic computational limitations, we have considered only the sequence fraction involving the first coordination sphere of the Cu(II) center and the segment of the second coordination including the mutated residue at the 41 position (Figure 5),[60,61] and for that reason, these computational results are qualitative in nature. Such a protein fragment constitutes the ET pathway connecting the solvent-exposed hydrophobic patch of the protein, that will be more accessible to the STM tip electrode,[14,29,62] and the active metal center. The protein folding structure of the fragment used for the electronic structure calculations (Figure 5) has been taken from the crystalline Wt structure[40] for both protein variants (Figure 1a). This is a good approximation given the minor disruption of the Cu coordination field after the outer-sphere mutation is performed, as deduced from our spectroscopic

DOI: 10.1021/jacs.7b06130
J. Am. Chem. Soc. 2017, 139, 15337−15346

characterization and MD simulations (Figure 1b–d). Fine structural analyses of the mutation effect will have to be considered for cases involving major structural changes in the mutant protein folding.[63]

In our single-protein junction experiments, the electrons are injected from the STM tip electrode into the Cu(II)-protein. Figure 5a shows the representation of the DFT-calculated LUMO frontier orbital for the ET-relevant fragment of the Wt azurin, showing significant LUMO contribution close to the metal center and its first coordination sphere in the oxidized state (Cu(II)) of the protein. The orbital energy values resulting from the DFT calculation (see the Supporting Information, section 7a) indicate that the energetic position of the LUMO fragment for this system (around −6 eV) is closer to the gold Fermi level (∼−5 eV) than the highest occupied molecular orbital (HOMO) fragment (positioned at lower energies than −7 eV). Assuming their uncertainty due to the self-interaction errors in DFT,[64,65] this suggests the LUMO fragment as the domination transport orbital. Such a statement is based on the assumption that the position of the energy levels in the considered protein fragment is not affected either by the presence of the rest of the protein or by the coupling with the gold electrodes. Although a transport calculation on the whole coupled system should be performed, this is computationally highly demanding and beyond the reach of state-of-the-art computational facilities. We believe that our assumption is based on a plausible scenario: in our MD simulations, the Cu ion is located at a distance of approximately 14 Å from the gold surface. At such a distance, molecular orbitals are expected to be decoupled from the electrodes and to be unaffected by both Coulomb screening effects[66] and by the electrostatic balance established at the interface.[67]

It is important to distinguish the orbital picture represented in Figure 5 from previously calculated orbitals of the redox Cu site of a metalloprotein. The latter corresponds to the well-established biological electron transfer field that describes the electron exchange with the metal center in a metalloprotein, which directly relates to the electrochemical response (Figure 1e). Such an orbital has been previously ascribed to a Cu(II)-SOMO.[60] Figure 5 instead is an attempt of describing electron transport across the entire protein when it bridges two metal leads in a nanoscale molecular device. Such a picture is intended to be captured by visualizing the low lying (closer to the electrodes' Fermi energy) molecular orbitals of the entire transport-relevant fragment of the protein in Figure 5.

As opposed to what is observed in the single-protein Wt junction, Figure 5b shows that the LUMO fragment in the K41C is mainly localized at the mutated *Cys*41 residue, with essentially no contribution near the Cu coordination sphere region. The LUMO distribution around the metal site evidences the implication of the protein redox state in the observed charge transport through the Wt protein, in agreement with a two-step sequential tunneling mechanism mediated by the metal redox center. We then hypothesize that the disappearance of the two-step sequential character in the K41C variant is caused by the lack of LUMO fragment distribution at the first Cu coordination sphere. The closest fragment orbital around the Cu center in the K41C variant appears now at the LUMO+2, further energetically separated, ∼1.5 eV (Supporting Information, section 7a), from the LUMO-fragment transport channel. This conclusion is supported by the similar transport behavior observed for a single-protein junction with an Apo (lack of Cu) variant (see the Supporting Information, section 5b). Within an ET pathway picture,[68] while both conduction channels, namely, sequential two-step (involving the redox metal center) and tunneling (nonredox), are present in the Wt single-protein electrical contact, the former is shut down in the K41C mutant case.[59,69] This conclusion is supported by the observed slower kinetics and anodically shifted electrochemistry for the K41C mutant (Figure 1e). The observed slower Cu(II)/Au electron transfer kinetics in the mutant foresees a larger energy penalty for the redox conduction channel (Cu redox signal) when electrons are transported through the entire protein junction, which translates into the non-Cu-mediated coherent tunneling being the dominant pathway in the K41C case. In an effort to rationalize the observed orbital transport picture with the redox properties of the metalloprotein, we suggest that the participation of the first Cu coordination sphere in the orbital transport channel, which can be tailored through protein mutagenesis, is a requirement to observe electrochemical conductance modulation in a single-protein junction.

CONCLUSIONS

We present a mechanistic analysis of bioengineered charge transport in a single-protein junction. We have exploited our static STM-based *blinking* approach[39] to transiently trap individual Cu-azurin metalloproteins between two metal leads and characterize their electrical properties as a function of the two key experimental parameters for charge transport for such redox molecular systems, namely, the electrochemical gate voltage and the temperature. The results prove that the conduction channels in the single-protein electrical contact can be finely tuned by performing point-site mutations in the outer protein structure involving mild structural changes in the protein backbone. In short, we have modified a wild-type *Pseudomonas aeruginosa* blue Cu-azurin at its secondary Cu coordination sphere (*Lys*41 residue) by introducing a *Cys*41 residue that caused minor structural modifications, as seen by both spectroscopy and MD simulations. Such minor structural changes have been ascribed to variations in the hydrophobicity and/or H-bonding network in the protein peptidic structure.[17] The slight reduction of charge density at the Cu center originated by the newly introduced *Cys*41 residue dramatically alters the charge transport behavior of the single-protein junction. Our MD simulations of the Au substrate/protein/STM tip junction suggest that the protein structure is preserved during our measurements, ruling out the possibility that these changes arise from any major structural rearrangement. The original two-step sequential charge transport in the Wt is shut down to give rise to a single-protein electrical contact displaying an almost fully coherent transport mechanism in the mutant, i.e., invariant to electrochemical gate voltage and temperature. Our DFT orbital calculations for the relevant segment to the protein transport (extracted from the crystallographic structure) suggest a simple yet intuitive explanation for the observed sharp transport transition, which is based on the lack of contribution of the first Cu coordination sphere in the transport-dominant frontier orbital for the modified protein. This interpretation should however be tested by a complete transport calculation on the metal–protein–metal system. Furthermore, the role of all the possible conformational changes due to thermal fluctuations, as predicted by the molecular dynamics simulations, in the transport mechanism should be investigated.

DOI: 10.1021/jacs.7b06130
J. Am. Chem. Soc. 2017, 139, 15337–15346

These results demonstrate the feasibility of tailoring the charge transport in a nanoscale biomolecular electrical contact and bring new horizons toward real bottom-up approaches to engineer the next generation of biosensors, biotransistors, or any platform requiring the optimization of the biomolecule/electrode electrical communication. The outcomes of this work go beyond a detailed interfacial study of the protein/electrode electrical contact. The observed abrupt transition in the ET behavior upon a single external mutation in the protein−protein "docking" patch of a functional redox protein points toward a plausible biological mechanism to control coherence in biological ET through minor structural/chemical changes. Similar mechanisms have been recently suggested in relevant bimolecular structures such as DNA.[70]

EXPERIMENTAL AND COMPUTATIONAL METHODS

A complete description of the mutagenesis procedures and characterization methodologies employed in this work has been included in the Supporting Information.

Spectroscopic Methods. The UV−vis absorption spectra were obtained at ambient temperature using an Infinite M200 PRO Multimode Microplate Reader from Tecan. Protein samples were approximately 7 μM protein in 50 mM ammonium acetate pH 4.5 buffer. Fluorescence spectra were recorded using a Horiba spectrofluorometer. The Trp48 fluorescence band, which has intrinsic fluorescence, was monitored after exciting at 290 nm. Both Wt and K41C variants were measured as well as their denaturized homologues.

Electrochemical Measurements. Cyclic voltammetry (CV) was undertaken using an Autolab PGSTAT-12 Galvanostat-Potentiostat (Metrohm Autolab). The three-electrode cell is composed by a platinum wire as a counter electrode, a miniaturized ultralow leakage membrane Ag/AgCl (SSC) as a reference electrode, and a $CH_3(CH_2)_5S$-functionalized Au(111) as a working electrode. All of the electrolyte solutions were deoxygenated with purified argon. To capture the protein CVs, the gold is immersed overnight in a 50 mM hexanethiol solution. Then, it is rinsed with abundant ethanol and water to remove the noncovalently bound hexanethiols. The functionalized Au is covered with a droplet of 50 mM ammonium acetate pH 4.5 containing the protein for at least 2 h. The azurin attaches to the hexanethiols by its hydrophobic patch near the copper ion (see the Supporting Information, section 4).

Electrochemical Scanning Tunnelling Microscopy (EC-STM). All experiments were performed with a PicoSPM microscope head and a PicoStat bipotentiostat (Agilent, USA) controlled by Dulcinea electronics (Nanotec Electronica, Spain) using the WSxM 4.13 software. Two different cells were used: a liquid cell with a standard sample plate for the room temperature measurements and a Peltier (Cold MAC) sample plate for temperature-controlled experiments. A four-electrode cell is required for the bipotentiostatic control: a Pt:Ir (80:20) wire as a counter electrode, a miniaturized ultralow leakage membrane Ag/AgCl (SSC) as a reference electrode, and the two working electrodes, a Au(111) substrate and a STM tip, whose potentials U_S and U_P, respectively, are expressed against the same Ag/AgCl reference electrode. A 50 mM ammonium acetate pH 4.55 buffer was used for the measurements, previously filtered and deoxygenated with an Ar stream. The EC-STM probes were mechanically cut from a 0.25 mm diameter Au wire (99.99%), and they are made of 1 cm in length, annealed with a butane flame, and coated with Apiezon wax to minimize leakage current when immersed in the working aqueous buffer. The leakage current of our tips was typically of <10 pA.[71]

Molecular Dynamics Simulations. All of the simulations were performed using the AMBER14 software suite[72] with NVIDIA GPU acceleration.[73−75] The parmbsc0 modification[76] of the Cornell ff99 force field[77] was used to describe all standard amino acids present in the azurin. The interatomic potentials of the copper atom and its corresponding five ligands were described using a force field derived from quantum mechanical simulations.[78] This force field has been widely used to model the blue-copper azurin protein.[18,79−81] In particular, recent experiments[80] have shown how early stages of mechanical unfolding of this protein are well described by this force field. In all of our simulations, the system is fully embedded in a water medium. The water is described using the explicit TIP3P model,[82] while Joung/Cheatham parameters were used to describe the sodium counterions.[83,84] For the gold atoms, we have resorted to the CHARMM-METAL force field,[85,86] since it is thermodynamically consistent with the AMBERFF used to describe the protein and it has been successfully employed to study inorganic−bioorganic interfaces.[86] We have used periodic boundary conditions and the particle mesh Ewald method (with standard defaults and a real-space cutoff of 10 Å) to account for long-range electrostatic interactions. van der Waals contacts were truncated at a real space cutoff of 10 Å for all of the simulations also. The SHAKE algorithm was used to constrain bonds containing hydrogen, thus allowing us to use an integration step of 2 fs. Coordinates were saved every 1000 steps.

Electronic Structure Calculations. The geometry of the Wt azurin structure was obtained from the PDB (1AZU code). The K41C geometry was based on 1AZU replacing the *Lys*41 for a *Cys*41. This structure is supported by spectroscopic measurements and molecular dynamic simulation (see main discussion). The calculated frontier orbitals for both protein fragments were obtained with *Density Functional* methods (DFT) using the software package *Gaussian 09*[87] and employing a long-range-corrected variant *CAM-B3LYP* method[88] and *6-311G+(d)* as basis set. The *ab initio* calculations were conducted in the protein fragments relevant to the ET involving the residues 41−45, 46, 112, 117, 121, and 129.

ASSOCIATED CONTENT

Supporting Information

The Supporting Information is available free of charge on the ACS Publications website at DOI: 10.1021/jacs.7b06130.

Chemicals and materials, K41C bioengineering methods, spectroscopic characterization, electrochemical tests, ECSTM technical details, TEM characterization of protein-conjugated NP, and computational details (PDF)

Molecular dynamics movie (MPG)

AUTHOR INFORMATION

Corresponding Authors

*ruben.perez@uam.es

*pau@icrea.cat

*isma_diez@ub.edu

ORCID

Linda A. Zotti: 0000-0002-5292-6759

Rubén Pérez: 0000-0001-5896-541X

Ismael Díez-Pérez: 0000-0003-0513-8888

Notes

The authors declare no competing financial interest.

ACKNOWLEDGMENTS

The plasmid pet3a carrying the azurin structural gene (Table S1) from *E. coli* was kindly provided from Dr. Jeff Warren (California Institute of Technology, Pasadena). We thank Prof. Eliseo Ruiz of the University of Barcelona for his support in the fluorescence characterization. We thank the financial support from the Spanish MINECO (projects MDM-2014-0377, CTQ2015-71406-ERC, CTQ2015-64579-C3-3-P, CTQ2016-80066R, RYC-2011-07951, CSD2010-00024, FIS2014-53488-P, MAT2014-54484-P, and MAT2014-58982-JIN), the COST Action MP1303, and the European Research Council (ERC) under the European Union's Horizon 2020 research and

DOI: 10.1021/jacs.7b06130
J. Am. Chem. Soc. 2017, 139, 15337−15346

innovation grant Agreement No. 681299. P.G. thanks EU Commission (ERANET SynBio MODULIGHTOR Project), Catalan Government (CERCA Programme and 2014SGR-1251 grant) and the Ramón Areces foundation. J.C.C. thanks the DFG and SFB 767 for sponsoring his stay at the University of Konstanz as Mercator Fellow. The authors thankfully acknowledge the computer resources, technical expertise, and assistance provided by the Red Española de Supercomputación (RES) at the Minotauro and Marenostrum supercomputers (BSC, Barcelona) and Altamira (IFCA, Santander) Supercomputers. We also acknowledge the support provided by the computing facilities of the Extremadura Research Centre for Advanced Technologies (CETA-CIEMAT), funded by the European Regional Development Fund (ERDF). CETA-CIEMAT belongs to CIEMAT and the Government of Spain.

REFERENCES

(1) Broda, E. *The Evolution of the Bioenergetic Processes*; Elsevier: Amsterdam, The Netherlands, 1975.
(2) *Progress in Inorganic Chemistry*; Lippard, S. J., Ed.; John Wiley & Sons, Inc.: Hoboken, NJ, 1984; Vol. *32*.
(3) Gray, H. B.; Winkler, J. R. *Proc. Natl. Acad. Sci. U. S. A.* **2005**, *102* (10), 3534.
(4) Sue, C. M.; Schon, E. A. *Brain Pathol.* **2000**, *10* (3), 442.
(5) Stadtman, E. R.; Berlett, B. S. *Drug Metab. Rev.* **1998**, *30* (2), 225.
(6) Gray, H. B.; Winkler, J. R. *Biochim. Biophys. Acta, Bioenerg.* **2010**, *1797* (9), 1563.
(7) Willner, I.; Katz, E. *Bioelectronics: from theory to applications*; Wiley-VCH: Weinheim, Germany, 2005.
(8) Zhang, A.; Lieber, C. M. *Chem. Rev.* **2016**, *116* (1), 215.
(9) Gray, H. B.; Winkler, J. R. *Annu. Rev. Biochem.* **1996**, *65*, 537.
(10) D'Amico, S.; Maruccio, G.; Visconti, P.; D'Amone, E.; Bramanti, A.; Cingolani, R.; Rinaldi, R. *IEE Proceedings - Nanobiotechnology*. IET Digital Library October 1, 2004; pp 173−175.
(11) Lee, T.; Kim, S.-U.; Min, J.; Choi, J.-W. *Adv. Mater.* **2010**, *22* (4), 510.
(12) Amdursky, N.; Marchak, D.; Sepunaru, L.; Pecht, I.; Sheves, M.; Cahen, D. *Adv. Mater.* **2014**, *26* (42), 7142.
(13) Gray, H. B.; Malmström, B. G.; Williams, R. J. P. *JBIC, J. Biol. Inorg. Chem.* **2000**, *5* (5), 551.
(14) Cascella, M.; Magistrato, A.; Tavernelli, I.; Carloni, P.; Rothlisberger, U. *Proc. Natl. Acad. Sci. U. S. A.* **2006**, *103* (52), 19641.
(15) Olsson, M. H. M.; Ryde, U.; Roos, B. O. *Protein Sci.* **1998**, *7*, 2659.
(16) Farver, O.; Marshall, N. M.; Wherland, S.; Lu, Y.; Pecht, I. *Proc. Natl. Acad. Sci. U. S. A.* **2013**, *110* (26), 10536.
(17) Marshall, N. M.; Garner, D. K.; Wilson, T. D.; Gao, Y.-G.; Robinson, H.; Nilges, M. J.; Lu, Y. *Nature* **2009**, *462* (7269), 113.
(18) Zanetti-Polzi, L.; Bortolotti, C. A.; Daidone, I.; Aschi, M.; Amadei, A.; Corni, S. *Org. Biomol. Chem.* **2015**, *13* (45), 11003.
(19) Springs, S. L.; Bass, S. E.; McLendon, G. L. *Biochemistry* **2000**, *39* (20), 6075.
(20) Clark, K. M.; Yu, Y.; Marshall, N. M.; Sieracki, N. A.; Nilges, M. J.; Blackburn, N. J.; van der Donk, W. A.; Lu, Y. *J. Am. Chem. Soc.* **2010**, *132* (29), 10093.
(21) Lancaster, K. M.; DeBeer George, S.; Yokoyama, K.; Richards, J. H.; Gray, H. B. *Nat. Chem.* **2009**, *1* (9), 711.
(22) Warren, J. J.; Lancaster, K. M.; Richards, J. H.; Gray, H. B. *J. Inorg. Biochem.* **2012**, *115*, 119.
(23) Lancaster, K. M.; Sproules, S.; Palmer, J. H.; Richards, J. H.; Gray, H. B. *J. Am. Chem. Soc.* **2010**, *132* (41), 14590.
(24) Mauk, A. G.; Moore, G. R. *JBIC, J. Biol. Inorg. Chem.* **1997**, *2* (1), 119.
(25) Sepunaru, L.; Pecht, I.; Sheves, M.; Cahen, D. *J. Am. Chem. Soc.* **2011**, *133* (8), 2421.
(26) Li, W.; Sepunaru, L.; Amdursky, N.; Cohen, S. R.; Pecht, I.; Sheves, M.; Cahen, D. *ACS Nano* **2012**, *6* (12), 10816.
(27) Yu, X.; Lovrincic, R.; Sepunaru, L.; Li, W.; Vilan, A.; Pecht, I.; Sheves, M.; Cahen, D. *ACS Nano* **2015**, *9* (10), 9955.
(28) Chi, Q.; Farver, O.; Ulstrup, J. *Proc. Natl. Acad. Sci. U. S. A.* **2005**, *102* (45), 16203.
(29) Chi, Q.; Zhang, J.; Andersen, J. E. T.; Ulstrup, J. *J. Phys. Chem. B* **2001**, *105* (20), 4669.
(30) Baldacchini, C.; Bizzarri, A. R.; Cannistraro, S. *Eur. Polym. J.* **2016**, *83*, 407.
(31) Baldacchini, C.; Kumar, V.; Bizzarri, A. R.; Cannistraro, S. *Appl. Phys. Lett.* **2015**, *106* (18), 183701.
(32) Della Pia, E. A.; Chi, Q.; Jones, D. D.; Macdonald, J. E.; Ulstrup, J.; Elliott, M. *Nano Lett.* **2011**, *11* (1), 176.
(33) Alessandrini, A.; Salerno, M.; Frabboni, S.; Facci, P. *Appl. Phys. Lett.* **2005**, *86* (13), 133902.
(34) Alessandrini, A.; Corni, S.; Facci, P.; Facci, P.; Sola, M.; Facci, P.; Facci, P.; Harris, G.; Lindsay, S. M. *Phys. Chem. Chem. Phys.* **2006**, *8* (38), 4383.
(35) Bâldea, I. *J. Phys. Chem. C* **2013**, *117* (48), 25798.
(36) Artés, J. M.; Díez-Pérez, I.; Gorostiza, P. *Nano Lett.* **2012**, *12* (6), 2679.
(37) Artés, J. M.; Lõpez-Martínez, M.; Díez-Pérez, I.; Sanz, F.; Gorostiza, P. *Small* **2014**, *10* (13), 2537.
(38) Díez-Pérez, I.; Hihath, J.; Lee, Y.; Yu, L.; Adamska, L.; Kozhushner, M. a; Oleynik, I. I.; Tao, N. *Nat. Chem.* **2009**, *1* (8), 635.
(39) Aragonès, A. C.; Haworth, N. L.; Darwish, N.; Ciampi, S.; Bloomfield, N. J.; Wallace, G. G.; Diez-Perez, I.; Coote, M. L. *Nature* **2016**, *531* (7592), 88.
(40) Adman, E. T.; Jensen, L. H. *Isr. J. Chem.* **1981**, *21*, 8.
(41) Garner, D. K.; Vaughan, M. D.; Hwang, H. J.; Savelieff, M. G.; Berry, S. M.; Honek, J. F.; Lu, Y. *J. Am. Chem. Soc.* **2006**, *128* (49), 15608.
(42) Bard, A. J.; Faulkner, L. R. *Electrochemical methods: fundamentals and applications*; Wiley: Weinheim, Germany, 2001.
(43) Huang, Q.; Quiñones, E. *Arch. Biochem. Biophys.* **2008**, *477* (1), 175.
(44) Artés, J. M.; López-Martínez, M.; Giraudet, A.; Díez-Pérez, I.; Sanz, F.; Gorostiza, P. *J. Am. Chem. Soc.* **2012**, *134* (50), 20218.
(45) Xu, B.; Tao, N. J. *Science* **2003**, *301* (5637), 1221.
(46) Hihath, J.; Xu, B.; Zhang, P.; Tao, N. *Proc. Natl. Acad. Sci. U. S. A.* **2005**, *102* (47), 16979.
(47) Artés, J. M.; Li, Y.; Qi, J.; Anantram, M. P.; Hihath, J. *Nat. Commun.* **2015**, *6*, 8870.
(48) Sek, S.; Misicka, A.; Swiatek, K.; Maicka, E. *J. Phys. Chem. B* **2006**, *110* (39), 19671.
(49) Scullion, L.; Doneux, T.; Bouffier, L.; Fernig, D. G.; Higgins, S. J.; Bethell, D.; Nichols, R. J. *J. Phys. Chem. C* **2011**, *115* (16), 8361.
(50) Haiss, W.; Wang, C.; Grace, I.; Batsanov, A. S.; Schiffrin, D. J.; Higgins, S. J.; Bryce, M. R.; Lambert, C. J.; Nichols, R. J. *Nat. Mater.* **2006**, *5* (12), 995.
(51) Chang, S.; He, J.; Kibel, A.; Lee, M.; Sankey, O.; Zhang, P.; Lindsay, S. *Nat. Nanotechnol.* **2009**, *4* (5), 297.
(52) Aragonès, A. C.; Darwish, N.; Saletra, W. J.; Pérez-García, L.; Sanz, F.; Puigmartí-Luis, J.; Amabilino, D. B.; Díez-Pérez, I. *Nano Lett.* **2014**, *14* (8), 4751.
(53) Pobelov, I. V.; Li, Z.; Wandlowski, T. *J. Am. Chem. Soc.* **2008**, *130* (47), 16045.
(54) Díez-Pérez, I.; Li, Z.; Guo, S.; Madden, C.; Huang, H.; Che, Y.; Yang, X.; Zang, L.; Tao, N. *ACS Nano* **2012**, *6* (8), 7044.
(55) Engelkes, V. B.; Beebe, J. M.; Frisbie, C. D. *J. Am. Chem. Soc.* **2004**, *126* (43), 14287.
(56) Hines, T.; Diez-Perez, I.; Hihath, J.; Liu, H.; Wang, Z. S.; Zhao, J.; Zhou, G.; Müllen, K.; Tao, N. *J. Am. Chem. Soc.* **2010**, *132* (33), 11658.
(57) Tsuji, A.; Kaneko, Y.; Takahashi, K.; Ogawa, M.; Goto, S. *Microbiol. Immunol.* **1982**, *26* (1), 15.
(58) Guzzi, R.; La Rosa, C.; Grasso, D.; Milardi, D.; Sportelli, L. *Biophys. Chem.* **1996**, *60* (1), 29.
(59) Migliore, A.; Nitzan, A. *J. Am. Chem. Soc.* **2013**, *135* (25), 9420.

DOI: 10.1021/jacs.7b06130
J. Am. Chem. Soc. 2017, 139, 15337−15346

(60) Solomon, E. I.; Szilagyi, R. K.; DeBeer George, S.; Basumallick, L. *Chem. Rev.* **2004**, *104* (2), 419.
(61) Blanco-Rodríguez, A. M.; Di Bilio, A. J.; Shih, C.; Museth, A. K.; Clark, I. P.; Towrie, M.; Cannizzo, A.; Sudhamsu, J.; Crane, B. R.; Sýkora, J.; Winkler, J. R.; Gray, H. B.; Záliš, S.; Vlček, A. *Chem. - Eur. J.* **2011**, *17* (19), 5350.
(62) Venkat, A. S.; Corni, S.; Di Felice, R. *Small* **2007**, *3* (8), 1431.
(63) Ghosh, S.; Xie, X.; Dey, A.; Sun, Y.; Scholes, C. P.; Solomon, E. I. *Proc. Natl. Acad. Sci. U. S. A.* **2009**, *106* (13), 4969.
(64) Rincón-García, L.; Ismael, A. K.; Evangeli, C.; Grace, I.; Rubio-Bollinger, G.; Porfyrakis, K.; Agraït, N.; Lambert, C. J. *Nat. Mater.* **2015**, *15* (3), 289.
(65) Kim, M.-C.; Sim, E.; Burke, K. *Phys. Rev. Lett.* **2013**, *111* (7), 73003.
(66) Stadler, R.; Geskin, V.; Cornil, J. *Phys. Rev. B: Condens. Matter Mater. Phys.* **2009**, *79* (11), 113408.
(67) Brooke, C.; Vezzoli, A.; Higgins, S. J.; Zotti, L. A.; Palacios, J. J.; Nichols, R. J. *Phys. Rev. B: Condens. Matter Mater. Phys.* **2015**, *91*, 195438.
(68) Beratan, D.; Onuchic, J.; Winkler; Gray, H. *Science* **1992**, *258* (5089), 1740.
(69) Garrigues, A. R.; Yuan, L.; Wang, L.; Mucciolo, E. R.; Thompon, D.; Del Barco, E.; Nijhuis, C. A. *Sci. Rep.* **2016**, *6*, 26517.
(70) Liu, C.; Xiang, L.; Zhang, Y.; Zhang, P.; Beratan, D. N.; Li, Y.; Tao, N. *Nat. Chem.* **2016**, *8* (10), 941.
(71) Güell, A. G.; Díez-Pérez, I.; Gorostiza, P.; Sanz, F. *Anal. Chem.* **2004**, *76* (17), 5218.
(72) http://ambermd.org/, 2014.
(73) Salomon-Ferrer, R.; Götz, A. W.; Poole, D.; Le Grand, S.; Walker, R. C. *J. Chem. Theory Comput.* **2013**, *9* (9), 3878.
(74) Götz, A. W.; Williamson, M. J.; Xu, D.; Poole, D.; Le Grand, S.; Walker, R. C. *J. Chem. Theory Comput.* **2012**, *8* (5), 1542.
(75) Le Grand, S.; Götz, A. W.; Walker, R. C. *Comput. Phys. Commun.* **2013**, *184* (2), 374.
(76) Pérez, A.; Marchán, I.; Svozil, D.; Sponer, J.; Cheatham, T. E.; Laughton, C. A.; Orozco, M. *Biophys. J.* **2007**, *92* (11), 3817.
(77) Cornell, W. D.; Cieplak, P.; Bayly, C. I.; Gould, I. R.; Merz, K. M.; Ferguson, D. M.; Spellmeyer, D. C.; Fox, T.; Caldwell, J. W.; Kollman, P. A. *J. Am. Chem. Soc.* **1995**, *117* (19), 5179.
(78) van den Bosch, M.; Swart, M.; Snijders, J. G.; Berendsen, H. J. C.; Mark, A. E.; Oostenbrink, C.; van Gunsteren, W. F.; Canters, G. W. *ChemBioChem* **2005**, *6* (4), 738.
(79) Paltrinieri, L.; Borsari, M.; Ranieri, A.; Battistuzzi, G.; Corni, S.; Bortolotti, C. A. *J. Phys. Chem. Lett.* **2013**, *4* (5), 710.
(80) Beedle, A. E. M.; Lezamiz, A.; Stirnemann, G.; Garcia-Manyes, S. *Nat. Commun.* **2015**, *6*, 7894.
(81) Zanetti-Polzi, L.; Corni, S.; Daidone, I.; Amadei, A. *Phys. Chem. Chem. Phys.* **2016**, *18* (27), 18450.
(82) Jorgensen, W. L.; Chandrasekhar, J.; Madura, J. D.; Impey, R. W.; Klein, M. L. *J. Chem. Phys.* **1983**, *79* (2), 926.
(83) Joung, I. S.; Cheatham, T. E. *J. Phys. Chem. B* **2009**, *113* (40), 13279.
(84) Li, P.; Roberts, B. P.; Chakravorty, D. K.; Merz, K. M. *J. Chem. Theory Comput.* **2013**, *9* (6), 2733.
(85) Heinz, H.; Lin, T.-J.; Kishore Mishra, R.; Emami, F. S. *Langmuir* **2013**, *29* (6), 1754.
(86) Heinz, H.; Ramezani-Dakhel, H. *Chem. Soc. Rev.* **2016**, *45* (2), 412.
(87) Frisch, M. J.; Trucks, G. W.; Schlegel, H. B.; Scuseria, G. E.; Robb, M. A.; Cheeseman, J. R.; Scalmani, G.; Barone, V.; Mennucci, B.; Petersson, G. A.; Nakatsuji, H.; Caricato, M.; Li, X.; Hratchian, H. P.; Izmaylov, A. F.; Bloino, J.; Zheng, G.; Sonnenberg, J. L.; Hada, M.; Ehara, M.; Toyota, K.; Fukuda, R.; Hasegawa, J.; Ishida, M.; Nakajima, T.; Honda, Y.; Kitao, O.; Nakai, H.; Vreven, T.; Montgomery, J. A., Jr.; Peralta, J. E.; Ogliaro, F.; Bearpark, M.; Heyd, J. J.; Brothers, E.; Kudin, K. N.; Staroverov, V. N.; Kobayashi, R.; Normand, J.; Raghavachari, K.; Rendell, A.; Burant, J. C.; Iyengar, S. S.; Tomasi, J.; Cossi, M.; Rega, N.; Millam, J. M.; Klene, M.; Knox, J. E.; Cross, J. B.; Bakken, V.; Adamo, C.; Jaramillo, J.; Gomperts, R.; Stratmann, R. E.; Yazyev, O.; Austin, A. J.; Cammi, R.; Pomelli, C.; Ochterski, J. W.; Martin, R. L.; Morokuma, K.; Zakrzewski, V. G.; Voth, G. A.; Salvador, P.; Dannenberg, J. J.; Dapprich, S.; Daniels, A. D.; Farkas, Ö.; Foresman, J. B.; Ortiz, J. V; Cioslowski, J.; Fox, D. J. *Gaussian 09*; Gaussian, Inc.: Wallingford, CT, 2009.
(88) Yanai, T.; Tew, D. P.; Handy, N. C. *Chem. Phys. Lett.* **2004**, *393* (1−3), 51.

DOI: 10.1021/jacs.7b06130
J. Am. Chem. Soc. 2017, 139, 15337−15346